Inorganic Chemistry

Article

pubs.acs.org/IC

Enantioselective Henry Reaction Catalyzed by "Ship in a Bottle" Complexes

Kusum K. Bania,[†] Galla V. Karunakar,[‡] Kommuru Goutham,[‡] and Ramesh C. Deka*[,†]

[†]Department of Chemical Sciences, Tezpur University, Napaam, Assam, India 784028

[‡]Division of Crop Protection Chemicals, Indian Institute of Chemical Technology, Uppal Road, Hyderabad, Andhra Pradesh, India 500007

Supporting Information

ABSTRACT: Two chiral Schiff-base complexes of copper(II) have been successfully encapsulated inside the cavity of zeolite-NaY via a "ship in a bottle" synthesis method. The presence of the two complexes inside the cages of zeolite-Y has been confirmed based on various spectrochemical and physicochemical techniques, viz. FTIR, UV−vis/DRS, ESR, XPS, CV, EDX, SEM, and TGA. Zeolite-encapsulated chiral copper(II) Schiff-base complexes are found to give a high-enantioselective (84% ee, *R* conformation) nitro-aldol product at −20 °C. The encapsulated copper complexes are found to show higher catalytic efficiency than their homogeneous counterparts under identical conditions. Density functional theory (DFT) calculation has been implemented to understand the effect of the zeolite matrix on structural, electronic, and reactivity properties of the synthesized complexes. Theoretical calculation predicts that upon encapsulation into the zeolite matrix the Cu center becomes more susceptible to nucleophilic attack, favoring a nitro-aldol reaction. A plausible mechanism is suggested based on the experimental and theoretical results. The structures of reaction intermediates and transition state(s) involved in the catalytic cycle are derived using DFT.

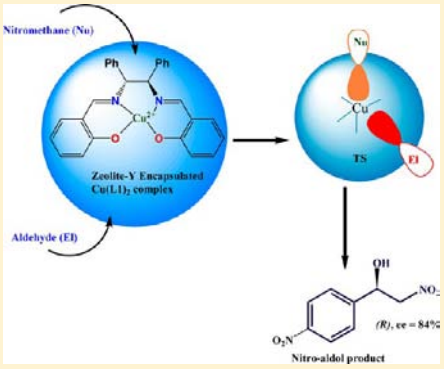

1. INTRODUCTION

Zeolite-encapsulated transition-metal and organometallic complexes have now emerged as some of the potent competitors for their homogeneous counterpart, in terms of catalytic behavior and stability.[1−6] The walls of the zeolite framework impart a constrained environment to the encapsulated, so-called "ship in a bottle", complexes.[7,8] The boundary or space constraint imposed by the zeolite walls changes the structural and electronic behavior of the encapsulated complexes in comparison to their homogeneous analogue.[9,10] These changes further influence their catalytic activities and, consequently, have fueled researchers to design more and more heterogeneous catalysts. In turn, this has resulted in a wide area of catalysis called "heterogenization of homogeneous catalyst".[11,12] There are several reports in which zeolite-encapsulated complexes have been found to exhibit better catalytic activity, high turnover number, and high thermal stability in comparison to their homogeneous counterpart.[13−16] Besides having the advantage of these hybrid materials in catalysis,[17] zeolite-encapsulated complexes have been currently studied to mimic the biosystem and hence are also named zeozymes.[18]

Finding a commercially viable pathway for the stereoselective organic synthesis of biologically important chemicals may be considered as one of the major thrust areas of chemistry today. Among the many routes attempted, those involving the use of chiral reagents and chiral catalysts are very important in the synthesis of effective drugs. The Henry reaction, commonly known as the nitroaldol condensation reaction, is one of the important C−C bond-formation reactions whose ultimate product has been used for various drug design.[19] Starting from Shibasaki et al.[20] and Evans et al.,[21] various chiral catalytic systems have been designed to bring out the enantioselective Henry reaction. Still, there remains a lot of scope to improvise this reaction.

Chiral Schiff bases and their complexes with transition metals are one of the most studied chiral catalysts[22] in asymmetric synthesis.[23,24] because of their ability to act as chiral catalysts or as cocatalysts, Schiff-base ligands as well as their complexes have been extensively applied either in the homogeneous phase or by anchoring them in various inorganic supports, viz., zeolite, MCM-41, clay, LDH, etc.[15,25−30] However, to best of our knowledge, the enantioselective Henry reaction performed by incorporating such types of chiral catalysts in zeolite-Y is sparse. So, considering the potentiality of chiral Schiff-base complexes, the advantages of the heterogeneous catalytic system, and the importance of the enantioselective Henry reactions, we have synthesized two Schiff-base complexes of copper (Scheme 1) inside zeolite-Y and tested these complexes for the enantioselective Henry reaction. Excellent yield and high enantioieselectivity have been obtained. Density functional theory (DFT) calculation has been applied to understand the nature of the structural and electronic changes that occur in the complexes under the influence of the zeolite framework. On the

Received: March 13, 2013
Published: July 2, 2013

   dx.doi.org/10.1021/ic400599c | *Inorg. Chem.* 2013, 52, 8017−8029

Scheme 1. Molecular Structures of (a) Ligand L1, (b) Ligand L2, (c) Cu(L1), and (d) Cu(L2) and Schematic Representation of Zeolite-Y-Incorporated (e) Cu(L1)-Y and (f) Cu(L2)-Y Complexes

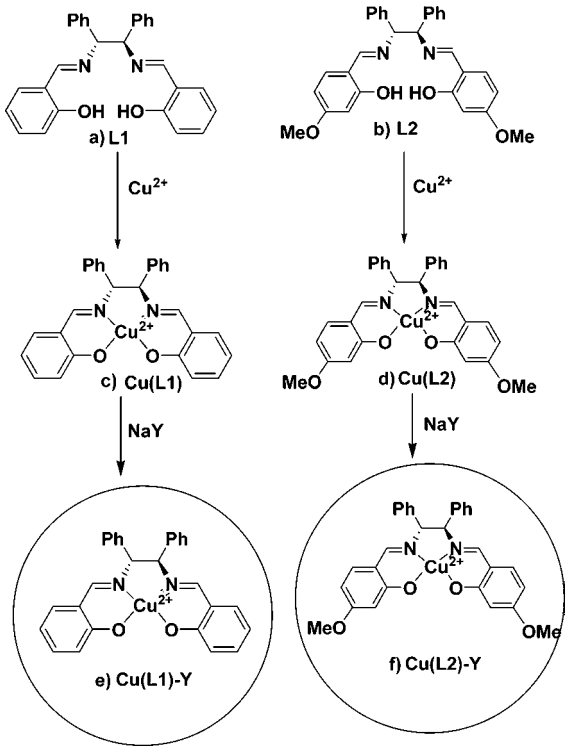

basis of theoretical and experimental evidence, a plausible mechanism has been suggested for the reaction catalyzed by such complexes.

2. EXPERIMENTAL AND THEORETICAL METHODS

The details of the materials used in this study, methods of synthesis of ligands L1 and L2 (Scheme S1), preparation of neat Cu(L1) and Cu(L2) and encapsulated copper chiral Schiff-base complexes Cu(L1)-Y and $Cu(L2)_2$-Y (Scheme S2), method of characterization, and theoretical calculations are provided in the Supporting Information.

3. RESULTS AND DISCUSSION

3.1. X-ray Diffraction (XRD) Study. The powder XRD pattern of the neat NaY, Cu^{2+}-exchanged zeolites and that of encapsulated complexes are shown in Figure 1. It can be observed from Figure 1 that, for pure zeolite-Y and for M^{2+}-exchanged zeolite-Y, the intensity of the I_{220} plane is greater than that of I_{311}, but for the encapsulated complex, the reverse is obtained, i.e., $I_{311} > I_{220}$. This reversal in the intensities has been empirically correlated with the presence of a large complex within the zeolite-Y supercage.[31] The above observation may therefore be construed as evidence for the successful encapsulation of copper Schiff-base complexes within the supercage of zeolite-Y.

3.2. Fourier Transform Infrared (FTIR) Spectroscopy. The FTIR spectra of NaY, metal-exchanged zeolite-Y, and neat and encapsulated Schiff-base complexes are shown in Figure 2. FTIR spectra of NaY and metal-exchanged zeolites show strong zeolite lattice bands in the range 500−1200 cm^{-1}. The strong and broad bands in the region 1010−1045 cm^{-1} could be attributed to the asymmetric stretching vibrations of $(Si/Al)O_4$ units. The broad bands in the regions 1650 and 3500 cm^{-1} are

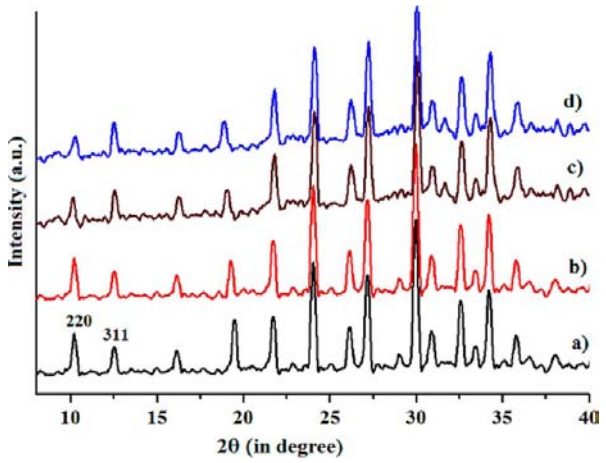

Figure 1. (a) XRD patterns of (a) pure zeolite-NaY, (b) Cu^{2+}-Y, (c) Cu(L1)-Y, and (d) Cu(L2)-Y.

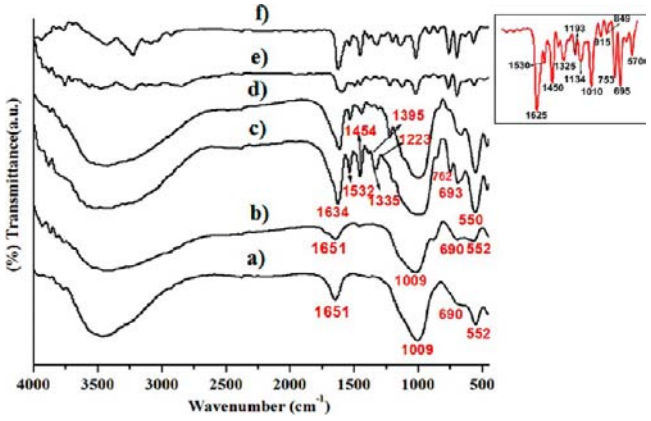

Figure 2. FTIR spectra of (a) NaY, (b) Cu^{2+}-exchanged zeolite, (c) Cu(L1)-Y, (d) Cu(L2)-Y, (e) Cu(L1), and (f) Cu(L2). The inset shows the peak values for the neat complexes in the region of 1650−500 cm^{-1}.

due to lattice water molecules and surface hydroxylic groups, respectively. The parent NaY zeolite shows characteristic bands at 552, 690, and 1009 cm^{-1} (Figure 2a) that are attributed to T−O bending mode, symmetric stretching, and antisymmetric vibrations, respectively.[32] No shift is observed upon introduction of the metal ions and upon encapsulation of the metal complexes (Figure 2b−d), which further implies that the zeolite framework has remained unchanged upon encapsulation of the complexes. The IR bands of all encapsulated complexes are weak because of their low concentration in the zeolite cage and thus can only absorb in the region of 1200−1600 cm^{-1}, where the zeolite matrix does not show any absorption band. The peak intensity of the zeolite-encapsulated complex may also occur because of strong interference of the bands associated with water. In other words, the bands of water might mask some of the weak bands in the encapsulated complex. In order to confirm this, we have taken the FTIR spectrum of the solid samples under vacuum after dehydration. The FTIR spectra of the dehydrated samples are shown in Figure 3. The FTIR spectra of the dehydrated samples are found to be much more intense, and no additional peak is observed in the region of 1200−1600 cm^{-1} (Figure 3, inset). IR spectra of the neat Schiff-base copper(II) complexes (Figure 2e,f) show major bands at 1625 (C═C), 1530 (C═N), 1450, 1325 (C−O), 753

dx.doi.org/10.1021/ic400599c | Inorg. Chem. 2013, 52, 8017−8029

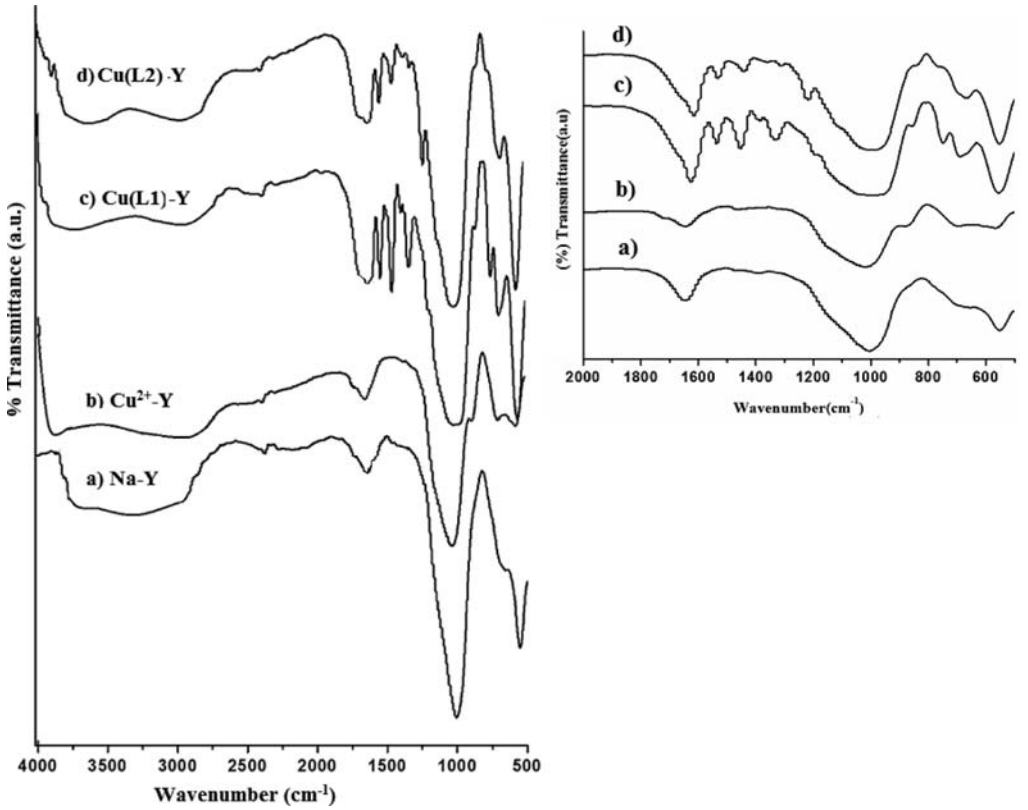

Figure 3. FTIR spectra of dehydrated samples taken under vacuum: (a) NaY; (b) Cu^{2+}-Y; (c) Cu(L1)-Y; (d) Cu(L2)-Y. The inset shows the expanded IR spectra of the solid samples in the region of 2000−500 cm^{-1}.

(ν_{C-H} aromatic ring) cm^{-1}. Similar frequencies are also observed in the case of zeolite-Y-encapsulated complexes with a little shift in the C═O, C═N, and C−O bands to wavenumbers 1634, 1532, 1454, and 1335 cm^{-1}, respectively, indicating nitrogen and oxygen coordination inside the cavity of the zeolite framework (Figures 2c,d and 3c,d). In addition to these bands, the encapsulated complexes also show a band at 1395 cm^{-1} corresponding to C−H deformation. These results give information for the formation of copper Schiff-base complexes in zeolite-Y.

3.3. UV−Vis/DRS Analysis. The UV−vis spectra of the Schiff-base ligands and their corresponding neat and zeolite-encapsulated copper complexes are depicted in Figure 4. The peaks are assigned in Table S1 in the Supporting Information. It is observed that the Schiff-base ligands give almost similar patterns of UV−vis peaks in water. Both ligand systems show five peaks nearly at 232, 262, 274, 340, 366, and 389 nm (Figure 4a,b). The first two higher-energy peaks are due to ligand-based $\pi \rightarrow \pi^*$, and the four lower-energy peaks are due to n $\rightarrow \pi^*$ transitions. The lower-energy bands at 262 and 274 nm in the case of ligands L1 and L2, respectively, correspond to the azomethyne group. The neat copper(II) complexes with ligands L1 and L2 show peaks above and below 250 nm due to $\pi \rightarrow \pi^*$ and n $\rightarrow \pi^*$ originating from the ligand system. Besides these, it also shows weak bands at 323, 377, and 384 nm, which can be attributed to metal-to-ligand charge transfer (MLCT). The comparison of the UV−vis spectra of the complexes with those of the free ligands indicates a blue shift in the $\pi \rightarrow \pi^*$ and n $\rightarrow \pi^*$ transitions. The shifting of the peaks toward higher-energy values and the appearance of MLCT transitions suggest formation of the copper complex.

The dehydrated Cu^{2+}-Y sample exhibits absorption bands at 636 and 710 nm, characteristic of the e $\rightarrow t_2$ and e $\rightarrow a_1$ transitions of the Cu^{II} ($3d^9$) ion in the trigonal site, respectively (see Figure S1 in the Supporting Information). The intense UV absorption component is attributed to charge-transfer excitation. The band at 253 nm is assigned to the ($3d^{10}$) $^1S_0 \rightarrow$ ($3d^9 4s^1$) $^2D_{5/2}$ configurational transition or may be due to interaction of the Cu^{2+} ion with the O atoms of zeolite. The second derivative of the peak gives absorption at 253 nm, which occurs as a shoulder in the DRS spectrum. This spectral behavior of the Cu^{2+}-exchanged zeolites indicates that the Cu^{2+} ion maintains a pseudotetrahedral environment of the type $(O_1)_3$-Cu^{2+}-L (where O = oxygen of the supercage of zeolite-Y).[8]

The diffuse-reflectance spectrometry (DRS) spectra of the encapsulated complexes are shown in Figure 4. It is observed from Figure 4d,e that the peaks are less intense than those of the corresponding neat complex, which may be due to the presence of a low concentration of metal complex inside the cavities. However, both complexes retain the same spectral regions as those in the neat complex. The only difference that can be observed from the peak values is that upon encapsulation the MLCT transitions significantly shifted to higher wavelengths (Figure 4g). The shifting of the spectral region toward lower-energy values may be due to the influence of the zeolite matrix on the electronic and structural properties of the encapsulated complex.

3.4. Electron Spin Resonance (ESR) Spectra. ESR spectra of the Cu^{2+}-exchanged zeolite, neat Schiff-base complexes, and encapsulated copper Schiff-base complexes are shown in Figure 5. ESR spectra for the neat complex as polycrystals are characterized by an axial **g** tensor. Hyperfine

dx.doi.org/10.1021/ic400599c | Inorg. Chem. 2013, 52, 8017−8029

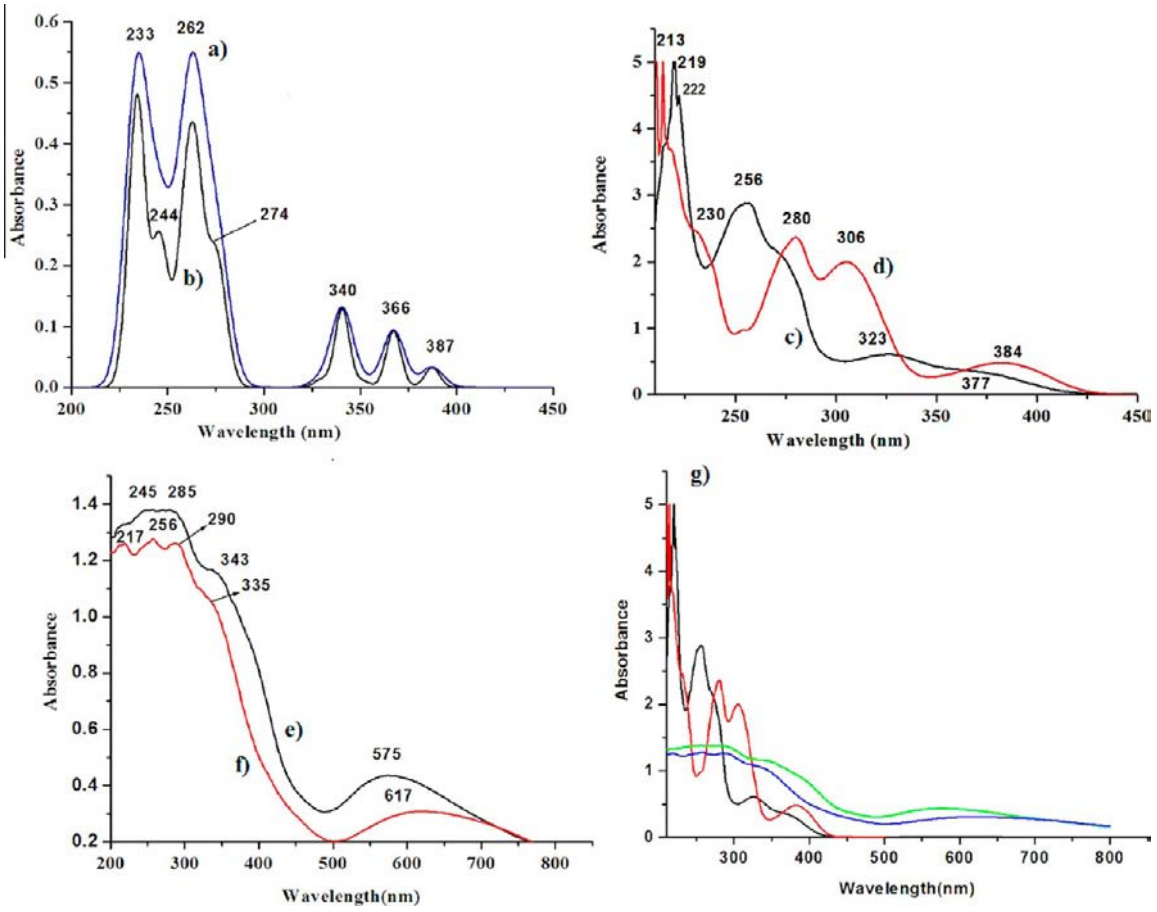

Figure 4. UV−vis/DRS spectra of (a) L1, (b) L2, (c) Cu(L1), (d) Cu(L2), (e) Cu(L1)-Y, and (f) Cu(L2)-Y and (g) a comparison of the absorption spectra of the neat and encapsulated complexes.

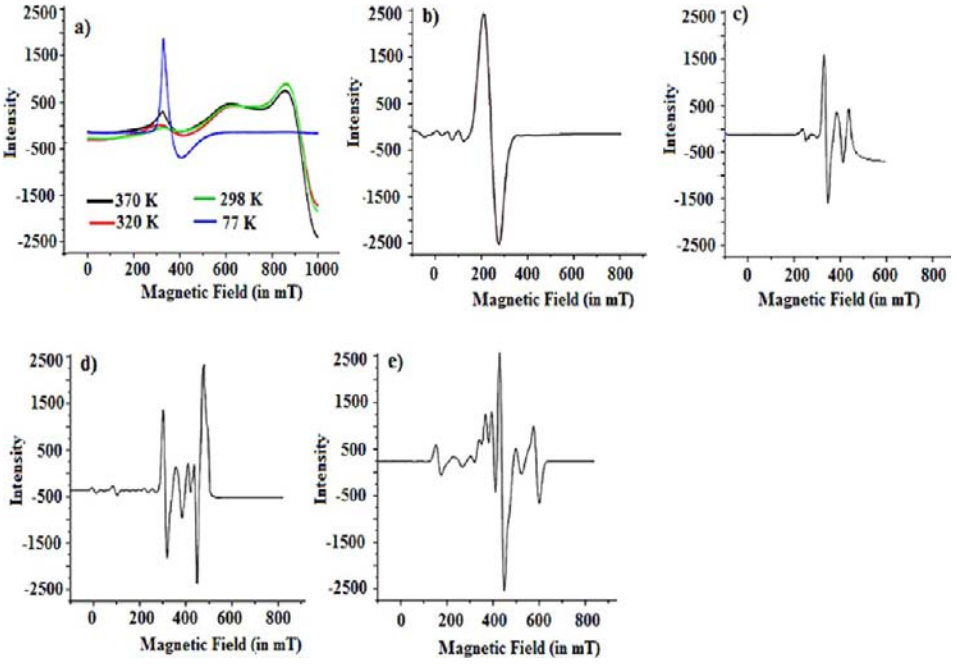

Figure 5. Powder EPR spectra of (a) Cu^{2+}Y taken at different temperatures, (b) neat Cu(L1), (c) neat Cu(L2), (d) encapsulated Cu(L1)-Y, and (e) Cu(L2)-Y complexes.

features for copper ($S = {}^1/_2$ and $I = {}^3/_2$) are observed at 77 K due to intermolecular spin−spin coupling for both the neat and encapsulated complexes. The ESR spectra of the neat copper Schiff-base complexes are shown in Figure 5b,c with two g

dx.doi.org/10.1021/ic400599c | Inorg. Chem. 2013, 52, 8017−8029

values [g_{II} = 2.450 and $g_{\perp}$ = 2.223 for Cu(L1)$_2$ and g_{II} = 2.420 and $g_{\perp}$ = 2.218 for Cu(L2)] that are characteristics of a normal tetragonal environment. The $g_{II} > g_{\perp} > 2.0023$ indicates that the unpaired electron is present in the $d_{x^2-y^2}$ orbital, which is characteristic of Cu ions that undergo tetragonal elongation. The four-line hyperfine signals in Cu^{2+}-Y at 250−400 mT are characteristic of the Cu nucleus with $I = {}^3/_2$. The encapsulated complexes show more than four lines of hyperfine signals due to interaction between the Cu nuclei and two equivalent ^{14}N atoms, indicating the presence of a copper(II) mononuclear complex inside zeolite (Figure 5d,e). The g_{II} values are found to be 2.227 for Cu(L1)-Y and 2.229 for Cu(L2)-Y and are less compared to the copper-exchanged NaY (g_{II}= 2.367). It is known that when the symmetry of the ligand field of the copper complex changes from octahedral via square-pyramidal coordination to a planar environment, the g_{II} value decreases. The decrease in the g value suggests the formation of a square-planar copper complex within the framework of zeolite-Y.

3.5. X-ray Photoelectron Spectroscopy (XPS). The location of the complexes in the zeolite cages can also be confirmed by XPS because it provides information about the relative concentrations of elements on the surface of ca. 40−50-Å-thick layers of the sample (ca. 1% of the crystal).[33] The XPS measurements are carried out for various copper Schiff-base complexes. It is found from a comparison of the signal intensities of the M_{2p} level (M = Cu) for the encapsulated samples and the metal-exchanged samples that the encapsulated complexes contain a lower concentration of the metal ions than NaY-metal-exchanged samples. The results obtained are in accordance with our energy-dispersive X-ray (EDX) and UV−vis studies. The decrease in the metal content in the encapsulated metal complexes can be attributed to the migration of noncomplexed metal ions during complex formation in the ship-in-a-bottle synthesis process. In addition to the information about the location of the complexes, some preliminary information about the oxidation states of the metal ion in both the neat and zeolite complexes can be obtained from the XPS data. Table 1 lists the binding energies for M 2p,

Table 1. XPS Analysis of the Metal-Exchanged Zeolite, Neat, and Encapsulated Complexes (M = Cu)

state	Cu(L1)	Cu(L2)	Cu(L1)-Y	Cu(L2)-Y	Cu^{2+}-Y
M $2p_{3/2}$	931.5	931.6	932.4	932.4	931.3
M $2p_{1/2}$	955.1	955.2	955.3	955.3	955.1
satellite	942.3	942.3	943.1	943.1	942.1
O 1s	531.4	531.4	529.9	529.9	531.4
N 1s	400.2	400.2	399.4	399.4	
C 1s (C−C)	284.6	284.6	284.6	284.6	
(O−C═O)	286.5	286.5	286.5	286.5	
Si 2s			154.0	154.0	154.0
Si 2p			102.9	102.9	103.0
Al 2p			74.4	74.4	74.5
Na 1s			1073.1	1073.1	1073.2

O 1s, N 1s, C 1s, Si 2s, Si 2p, Al 2p, and Na 1s in various copper Schiff-base complexes. In all of the Schiff-base complexes (both neat and encapsulated), two different kinds of C atoms (C−C, 284.6 eV; C−O, 286.5 eV) and only one kind of N atom (399.2 eV) are observed (Figure S2(ii) in the Supporting Information). The core-level photoelectron peaks of the neat and encapsulated complexes as well of the metal-exchanged zeolites are assigned in Figure S2(i) in the Supporting Information. The presence of Cu^{2+} is confirmed by the Cu $2p_{3/2}$ and Cu $2p_{1/2}$ peaks at 932.4 and 955.2 eV, respectively, accompanied by a relatively low intense satellite peak at 942.3 eV. These values are in accordance with the previously reported binding energy value for copper.[34] It can be observed from Table 1 that in all of the samples the binding energies of Si 2s, Al 2p, and Na 1s remain unchanged. However, small shifts toward higher energies for M 2p and toward lower energy for O 1s and N 1s are observed in all of the encapsulated complexes. The high M $2p_{3/2}$ binding energy found in [M(L)]Y indicates the presence of Schiff-base complexes inside zeolite-Y. This is attributed to the fact that upon encapsulation the charge density on the metal centers decreases, which could be due to impairment of delocalization of the π electrons of the ring when the complexes are confined inside the zeolite cavity.[35]

3.6. Cyclic Voltammetry (CV) Study. The electron-transfer processes associated with the electroactive species located in the interior part of the microporous material have gained substantial interest in recent years.[36] However, the exact electron-transfer mechanism is still a matter of debate in some cases.[37] Shaw et al.[38] first proposed two possible mechanisms, intrazeolite and extrazeolite (eqs 1 and 2, respectively), for electron transfer associated with encapsulated transition-metal complexes within the supercage of zeolite and surface-bound metal complexes, respectively, based on zeolite-modified electrodes (ZMEs).

Intrazeolite mechanism

$$E_z^{\,m} + ne^- + nC(s)^+ \leftrightarrow E_z^{\,(m-n)+} + nC(z)^+ \quad (1)$$

Extrazeolite mechanism

$$E_z^{\,m+} + mC(s)^+ \leftrightarrow E(s)^{m+} + mC(z)^+$$

$$E(s)^{m+} + ne^- \leftrightarrow E(s)^{(m-n)+} \quad (2)$$

where E^{m+} = an electroactive probe, z = zeolite, s = solution phase, and C^+ = an electrolyte cation.

Besides the two possible electron-transfer mechanisms, Dutta and Ledney[39] have proposed three distinct pathways of charge transfer in ZMEs, which is an extension of the original models proposed by Shaw et al. Doménech et al.[40] have also proposed the following mechanism for a zeolite-Y-associated Mn(salen)-N_3 complex.

$$Mn^{III}(salen)N_3(sol) + e^- = Mn^{II}(salen)N_3(sol) \quad (3)$$

The reduction of boundary-associated complexes can yield species in solution

$$Mn^{III}(salen)N_3(b) + M^+(sol) + e^- = Mn^{II}(salen)N_3^-(sol) + M^+(b) \quad (4)$$

or involve the electron-transfer process to a zeolite-associated species:

$$Mn^{III}(salen)N_3(b) + M^+(sol) + e^- = Mn^{II}(salen)N_3^-(b) + M^+(b) \quad (5)$$

where (sol) represents species in the solution phase and (b) is for boundary-associated species. M^+ represents the charge-balancing cation of the supporting electrolyte. On the basis of the above mechanism and electrochemical behavior, they propose an extrazeolite electron-transport process and the

dx.doi.org/10.1021/ic400599c | Inorg. Chem. 2013, 52, 8017−8029

Table 2. Elemental Analysis for NaY, Cu^{2+}-Y, Cu(L1)-Y, and Cu(L2)-Y

	EDX analysis (wt %)						AAS (wt %)			CHN analysis (wt %)		
sample	Si	Al	Na	M	C	N	Al	Na	M	C	N	H
NaY	21.42	8.57	7.55				8.59	7.58				
Cu^{2+}-Y	21.46	8.44	6.74	0.94			8.48	6.56	0.93			
Cu(L1)-Y	21.80	8.20	5.65	0.72	20.80	1.44	8.23	5.45	0.73	21.80	1.46	18.70
Cu(L2)-Y	21.40	8.80	5.35	0.76	19.75	1.49	8.76	5.38	0.77	20.15	1.52	21.85

Table 3. Calculated Energies of the HOMO and LUMO Levels (in eV), Chemical Potential (μ, in eV), Global Hardness (η, in eV), Electrophilicity Index (ω, in eV), and Softness (S, in eV)[a]

complex	IP	EA	HOMO	LUMO	μ	η	ω	S
Cu(L1)(↑)	2.419	1.221	−4.438	−2.341	−3.389 (−1.820)	1.048 (0.599)	5.478 (2.764)	0.476 (0.834)
Cu(L1)(↓)			−4.478	−2.633	−3.555	0.9225	6.851	0.542
Cu(L2)(↑)	2.843	1.834	−4.171	−2.440	−3.305 (−2.339)	0.865 (0.504)	6.312 (5.423)	0.577 (0.991)
Cu(L2)(↓)			−4.664	−3.052	−3.858	0.806	9.233	0.620
Cu(L1)-Y(↑)	5.176	4.428	−3.917	−2.440	−3.178 (−4.802)	0.738 (0.374)	6.840 (30.838)	0.677 (1.336)
Cu(L1)-Y(↓)			−3.322	−2.118	−2.72	0.602	6.144	0.830
Cu(L2)-Y(↑)	4.922	4.151	−3.936	−2.416	−3.17 (−4.537)	0.76 (0.385)	6.636 (26.690)	0.657 (1.296)
Cu(L2)-Y(↓)			−3.268	−1.963	−2.615	0.652	5.242	0.766

[a]The values given in parentheses are those obtained by using the IP and EA values.

existence of topological redox isomers of the Mn(salen)N_3 complex.

Although these mechanistic assignments are controversial, there are various reports demonstrating the redox behavior of transition-metal complexes encapsulated in zeolite cavities.[41−43]

Cyclic voltammograms of zeolite-encapsulated complexes taken as a part of ZME in the presence of 0.1 M TBAP as the supporting electrolyte are shown in Figure S3 in the Supporting Information. It has been reported that electrochemical analysis of chemically modified zeolite is much more reliable unless the crystallinity of the zeolites get ruptured during the preparation of ZME.[44] The cyclic voltammograms of the neat complexes Cu(L1) and Cu(L2) taken in solution mode are shown in parts a and b of Figure S3 in the Supporting Information, respectively. It is observed that Cu(L1) shows two reduction potentials (Table S2 in the Supporting Information). The first wave corresponds to the electrochemically quasi-reversible Cu^{II}/Cu^{I} transition, whereas the second one features a reduction of Cu^{I} to the corresponding Cu^{0}, followed by removal of the metal center from the Schiff-base ligand. It also shows two oxidation peaks corresponding to Cu^{0}/Cu^{I} and Cu^{I}/Cu^{II} couples. Similar to Cu(L1), the Cu(L2) complex also shows two reduction and two oxidation peaks (Figure S3b in the Supporting Information). The difference in redox potential values in the two complexes indicates that substitution at the phenyl ring greatly influences the electrochemical behavior. The cyclic voltammograms of encapsulated complexes as a part of ZME are shown in Figure S3c in the Supporting Information. The peak current remains stable more than 6 h, indicating the stability of the complexes inside the cavity of the zeolite. These redox potential values are completely different from that of the Cu^{2+}-exchanged zeolite-Y,[8] indicating the formation of Schiff-base complexes inside zeolite-Y. It can be observed from Figure S3c and Table S2 in the Supporting Information that upon encapsulation the peaks are broadened and the average reduction potential values of Cu(L1)-Y get shifted toward more negative values, whereas that of Cu(L2)-Y is shifted to more positive values. The shifting of the reduction potential value toward a more negative value in the case of Cu(L1)-Y indicates stabilization of the Cu^{II} oxidation state in zeolite cages.[45] Electrochemical analysis of zeolite-encapsulated complexes based on ZME depends on the preparation of the modified electrode. It may so happen that during modification or pressing of the sample the crystallinity of the zeolite may get ruptured and the voltammogram so obtained may not be apparent because of encapsulated complexes. This may be due to disintegration of the complexes over the zeolite surface. In order to confirm this, we again perform XRD and DRS analysis of the samples after the CV study. We obtain the same pattern of XRD and DRS spectra as we obtained before it was subjected to ZME. So, it can be concluded that during the preparation of ZME the zeolite structures are not ruptured and the redox behavior is due to the presence of a redox-active copper Schiff-base complex present in the cavities of zeolite-Y.

3.7. Elemental Analysis. Elemental (Cu, C, N, O, Al, Na, and Si) detection has been performed by EDX (Figure S4 in the Supporting Information), atomic absorption spectroscopy (AAS), and CHN analyses. The amount of metal content in the synthesized complexes has also been determined by Vogel's method[46] for comparison with the above elemental analyses. Complete elemental analysis data are given in Table 2. It is found from elemental analyses that the Si/Al ratio in the virgin NaY is found to be ∼2.5. This ratio remains almost constant in all of the prepared samples, indicating the absence of dealumination either upon metal exchange or upon encapsulation of the copper Schiff-base complexes. Chemical analyses of the encapsulated samples reveal the presence of a metal complex, Cu(L), with Cu/C and Cu/N ratios roughly similar to the theoretical values of 0.035 and 0.5, respectively, for pure complexes. It can be observed from Table 3 that the loadings of the metal into the ion-exchanged zeolite and zeolite-encapsulated complexes are quite close in value to each other, which suggests that almost all of the metal ions present in the zeolite lattice get complexed and the uncomplexed metal ions are removed during back-exchange by refluxing with 0.01 M NaCl. The small percentage of metal that remains uncomplexed may be metal ions trapped in the cage by the complex formed around it or may be leached out during encapsulation of the complex. This is quite similar to that of manganese leaching after the introduction of salen ligands into

dx.doi.org/10.1021/ic400599c | Inorg. Chem. 2013, 52, 8017−8029

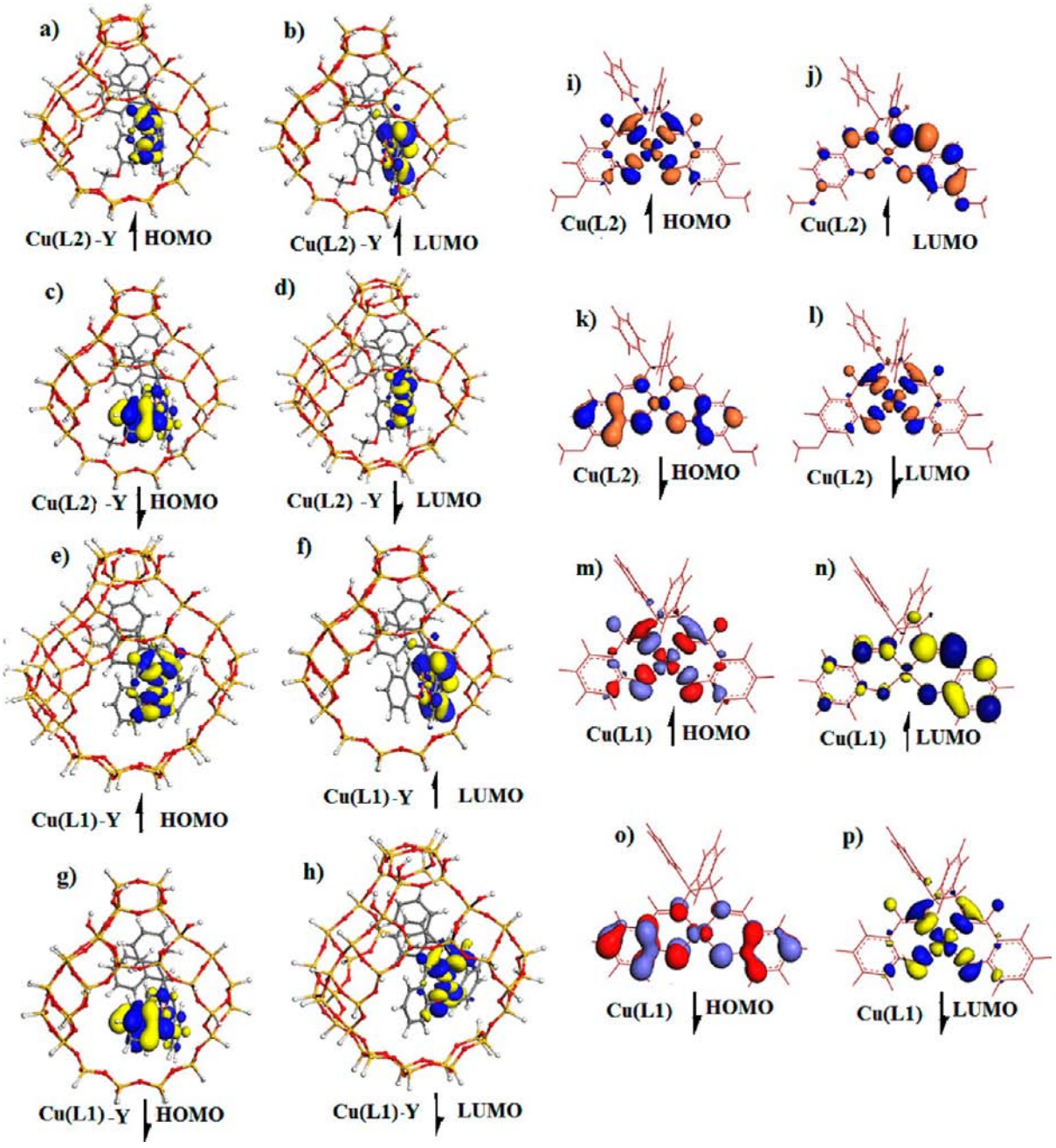

Figure 6. HOMO and LUMO orbitals of the neat and encapsulated copper(II) Schiff-base complexes. The arrows in parentheses indicate the HOMO and LUMO orbitals with spin-up (↑) and spin-down (↓) states.

zeolite-Y.[47] These traces of uncomplexed metal ions are unlikely to cause any serious interference in the behavior of the encapsulated complexes.

3.8. Scanning Electron Microscopy (SEM). SEM micrographs of complexes taken before Soxhlet extraction and those taken after Soxhlet extraction are shown in Figure S5 in the Supporting Information. The SEM taken before purification shows the presence of some unreacted or extraneous particles on the external surface. In the SEM of finished products, no surface complexes are seen and the particle boundaries on the external surface of zeolite are clearly distinguishable. This is much clearer from the surface plot shown in Figure S6 in the Supporting Information. Homogeneous surface morphology for the neat NaY zeolite and the samples after Soxhlet extraction respectively are observed in parts a, d, and e of Figure S6 in the Supporting Information. The surface plot for the samples before Soxhlet extraction, however, is found to be non-homogeneous, indicating that the surface is being occupied by extraneous complexes or the uncomplexed ligands. The presence of similar surface morphology before and after encapsulation into zeolite-Y confirms that encapsulation has not affected the surface crystallinity. Further, it also indicates the efficiency of the purification procedure to effect complete removal of extraneous complexes, leading to well-defined encapsulation in the cavity.

3.9. Thermogravimetric Analysis (TGA). TGA plots of the neat copper(II) Schiff base and the encapsulated complexes are shown in Figure S7 in the Supporting Information. The two neat complexes show peaks below 100 °C, which is due to elimination of the outer-sphere water molecule (Figure S7,

dx.doi.org/10.1021/ic400599c | Inorg. Chem. 2013, 52, 8017−8029

curves a and b, in the Supporting Information). The peaks above 300 °C are due to partial decomposition of the complexes. The weight losses at the higher temperature range 350−550 °C are due to complete decomposition of the sample.[48] A comparison of TGA for neat complexes with the encapsulated ones shows that these complexes become more stable once they get embedded inside the cavity of zeolite-Y (Figure S7, curves c and d, in the Supporting Information). In the case of the encapsulated metal complexes, the weight losses due to partial decomposition occur at lower temperature; however, they do not undergo complete decomposition up to 700 °C. This indicates that the two chiral copper(II) complexes become somewhat more stable upon encapsulation.

3.10. Theoretical Calculation. *3.10.1. Geometries.* The geometrical parameters obtained from VWN/DN level calculations for the neat and encapsulated complexes are provided in Table S3 in the Supporting Information. The calculated bond lengths and bond angles for the neat complexes are found to be in good agreement with the similarly reported Schiff-base complex of copper. After encapsulation of the chelated copper Schiff-base complexes, the bond lengths and bond angles are found to differ slightly in comparison to those of the neat complexes. This indicates that, upon encapsulation into the zeolite framework, the complex has not undergone much more distortion, which may change the active site in the complexes. Furthermore, we have also calculated the volume of the zeolite cluster model and the neat complexes using *MaterialsStudio* software.[49] The calculated volume of the zeolite supercage (1150.35 Å^3) is found to be sufficient enough to hold the two Schiff-base complexes having volumes of Cu(L1) = 410.53 Å^3 and Cu(L2) = 462.70 Å^3.

3.10.2. Electronic Structure, Ionization Potential (IP), Electron Affinity (EA), and Binding Energy. A schematic representation of the frontier molecular orbital for the neat and encapsulated complexes is shown in Figure 6. For all of the complexes, the patterns of the occupied and unoccupied orbitals are qualitatively similar. Copper(II) is an open-shell system with a d^9 configuration; hence, we performed spin-unrestricted calculations on all of the systems. The energies of the highest occupied molecular orbital (HOMO) and lowest unoccupied molecular orbital (LUMO) orbitals corresponding to spin-up and spin-down states are found to be different in both the neat and encapsulated systems. The energy values for the frontier orbital of all four systems are given in Table 3. It can be seen from Table 3 that the HOMO and LUMO orbitals of the encapsulated complexes lie higher in energy in comparison to those of the neat complexes. The IP and EA values are also found to increase upon encapsulation. However, the HOMO−LUMO gaps and the differences between IP and EA in the encapsulated complexes are found to decrease in comparison to those of the free complexes. Among the encapsulated systems, the HOMO energy of Cu(L1)-Y (with the spin-down state) is much higher-lying and the LUMO of Cu(L1)-Y with the spin-up state is much lower-lying. In the neat complexes, Cu(L2) with the spin-up state has the higher-lying HOMO, whereas its spin-down state has the lower-lying LUMO. This change in the HOMO and LUMO energies further signifies the effect of encapsulation on the orbital energies of the copper Schiff-base complexes. We have also calculated the interaction energy of the encapsulated complexes as the energy differences between the optimized encapsulated complexes and the corresponding fragments (neat metal complex and the zeolite framework) optimized as isolated molecules. The calculations of the interaction energy at the same level of theory are found to be in the order of Cu(L1)-Y (32.02 eV) < Cu(L2)-Y (36.83 eV). This result indicates that the Cu(L2) complex interacts more strongly and becomes more stabilized than the other complexes. This difference in interaction energy can be attributed to a change in the geometrical parameters and the presence of a bulkier group in the phenyl ring. These differences in the interaction energy bring a considerable change in the energies of the HOMO and the LUMO levels.

3.10.3. Global Descriptors. We have also calculated the DFT-based global descriptors, viz., chemical hardness (η), chemical potential (μ), electrophilicity index (ω), and softness (S), using a DN basis set and VWN functional for the neat and encapsulated complexes. The values for η, μ, ω, and S given in Table 3 are calculated based on two approximations, Koopmans' and finite difference. According to Koopmans' approximation, IP is the negative of the HOMO energy and EA is the negative of the LUMO energy. The plot of IP and EA against the HOMO and LUMO energies of the spin-down state, respectively, shows a linear correlation with regression r^2 values of 0.988 and 0.923 (Figure S8 in the Supporting Information). Because of several limitations associated with Koopmans' approximation,[50−53] especially in the case of transition-metal complexes, numerical values of η, S, and ω obtained from both approximations are found to be different. However, the trend in the change of the global descriptor values predicted by both approximations for the considered systems follows the same order. For example, the change in the global hardness values predicted by eqs 1 and 2 as well as by eqs 5 and 6 (see the Supporting Information) follows the same order, i.e., Cu(L2) < Cu(L1) for the neat complexes and the reverse for the encapsulated complexes.

According to the maximum hardness principle (MHP),[54,55] the most stable structure has the maximum hardness. Thus, the neat complexes with maximum hardness are chemically more stable compared to the encapsulated ones. Further, it can be seen from Table 3 that upon encapsulation both values of the chemical potential (μ) increase, whereas that of the electrophilicity index (ω) is found to increase in the case of the spin-up state but decreases in the case of the spin-down state. This result suggests that the occupancy of the electron, i.e., whether it involves an α orbital or a β orbital, will also bring out a considerable change in the reactivity of the system. In this context, it is pertinent to mention that the electrophilicity containing information for both electron transfer (chemical potential) and stability (hardness) can be considered to be a better descriptor of the global chemical reactivity. Moreover, ω includes a hardness term in the denominator, which is a descriptor of the stability. The electrophilicity is expected to exhibit an inverse linear relationship with hardness, or in correlation with MHP, we can say that under the conditions for the existence of an MHP, there will also be a *minimum electrophilicity principle*.[56] We have observed from our calculation that, in the case of neat complexes, Cu(L1) with maximum hardness has a minimum electrophilicity and the same is true in the case of the encapsulated Cu(L2)-Y complex (Table 3). Thus, it is found that upon encapsulation of the complexes into the zeolite framework the chemical potential (μ) and global softness (S) values increase, whereas that of η decreases. This change in the values of the global descriptors reflects the effect of the zeolite matrix on the reactivity of the complexes, and it can be said that complexes with high μ values

dx.doi.org/10.1021/ic400599c | Inorg. Chem. 2013, 52, 8017−8029

Table 4. Results of the Henry Reaction in the Presence of Various Catalysts[a]

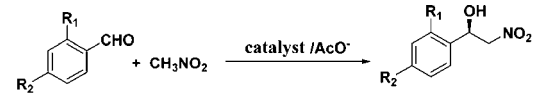

1a R_1= H, R_2 = H
1b R_1= H, R_2 = NO_2
1c, R_1= NO_2, R_2= H
1d, R_1= H, R_2= CH_3
1e, R_1=H R_2= OH
1f, Napthaldehyde

2a R_1= H, R_2 = H
2b R1= H, R_2 = NO_2
2c, R_1= NO_2, R_2= H
2d, R_1= H, R_2= CH_3
2e, R_1=H R_2= OH
2f, 1-(naphthalen-6-yl)-2-nitroethanol

		NaY		Cu^{2+}-Y		Cu(L1)		Cu(L2)		Cu(L1)-Y		Cu(L2)-Y	
reactant	product	yield (%)	ee (%)	yield (%)	ee (%)	yield (%)	ee (%)	yield (%)	ee (%)	yield (%)	ee (%)	yield (%)	ee (%)
1a	**2a**	48 (36)		63 (28)		82 (24)	62	80 (24)	61	92 (18)	82	90 (18)	80
1b	**2b**	50 (32)		66 (22)		89 (22)	67	84 (22)	72	96 (16)	84	95 (16)	83
1c	**2c**	54 (32)		68 (22)		87 (21)	76	88 (21)	74	94 (17)	84	93 (17)	82
1d	**2d**	53 (34)		64 (26)		78 (25)	72	86 (25)	66	93 (19)	78	86 (19)	79
1e	**2e**	49 (38)		58 (30)		82 (24)	64	77 (24)	60	88 (20)	74	82 (20)	76
1f	**2f**	47 (38)		52 (29)		83 (26)	60	82 (26)	68	82 (22)	73	84 (22)	74

[a]The values given in parentheses are the time (in h) required for completion of the reaction. Reactions are conducted at 1 mmol scale employing 5 equiv of nitromethane in ethanol. Reactions are carried out at −20 °C using 10 mg of the catalyst. The values (% ee, *R* isomer) are calculated from HPLC analysis.

can actively participate in electron-transfer reactions. In our case, the Cu(L1)-Y complex with minimum η and maximum S values will be the most reactive system.

3.10.4. Local Descriptors. Table S4 in the Supporting Information presents the Fukui functions (FFs; f_κ^+ and f_κ^-) for the selected metal atoms and the coordinated N atoms calculated using a Hirshfeld population analysis (HPA) scheme for the neat and encapsulated metal complexes. It is seen in Table S4 in the Supporting Information that the values of the FFs at the metal centers increase upon encapsulation. Thus, the zeolite framework modifies the reactivity of the metal atom from a less electrophilic or nucleophilic site in neat complexes to a higher site in encapsulated ones. As far as the attack of a nucleophile or electrophile at a particular site is concerned, the Cu atom (in both neat and encapsulated complexes) possessing the higher value of FFs (f_κ^+ and f_κ^-) will be the most preferential site. A comparison of the FFs (at the metal center) between the encapsulated and neat complexes suggests that a nucleophile will preferentially attack the Cu center in the encapsulated complexes. This further indicates that encapsulated complexes can actively participate in a base-catalyzed reaction.

3.10.5. Spin Density Calculation. The considered copper(II) complexes are open-shell systems with copper at the d^9 electronic configuration. The electronic configuration suggests that the excess spin density should be localized on the Cu center. The spin density calculation on the two neat complexes using *DMOL*[3] program at the VWN/DN level of theory indicates that, in both complexes, a high percentage (more than 50% of the total Mullikan charge density) is concentrated on the central Cu atom (Figure S9 in the Supporting Information). A substantial minority spin density is located on coordinated N and O atoms (10−11% of the total Mullikan charge density). This minority spin density results from the slight spatial offset between the α- and β-spin forms of the d_π−p_π molecular orbitals. The presence of the high-spin density on the metallic center implies that the unpaired d electron is mostly concentrated on the metallic center and is not delocalized over the aromatic rings of the coordinating ligands.

3.11. Catalytic Study. To test the catalytic efficiency of the synthesized complex, we choose *p*-nitrobenzaldehyde as the test substrate and compared it with copper(II) acetate. In the case of heterogeneous catalysis, a 0.01 M solution of acetic acid is used to generate the nitronate ion from nitromethane. Because acetic acid exists as $CH_3COOH \rightarrow CH_3COO^- + H^+$, the conjugate base, i.e., CH_3COO^-, will react with some amount of sodium species of NaY to form CH_3COONa.[56] The resulting CH_3COONa will act as the proton-abstracting source, thereby generating the nitronate ion ($CH_2NO_2^-$) from nitromethane (CH_3NO_2).

The reactivity and enantioselectivity of the nitroaldol reaction is strongly dependent on the nature of the solvent used. Therefore, a catalytic enantioselective Henry reaction is conducted in different solvents, such as toluene, 1,2-dichloromethane, tetrahydrofuran, CH_3CN, ethanol, and methanol, with catalyst Cu(L1)-Y under identical reaction conditions. It can be seen in Table S5 in the Supporting Information that polar solvents give better yield and high enantioselectivity in comparison to the nonpolar ones. In the present case, we found ethanol as the best solvent system; in terms of productivity and enantioselectivity, hence we performed all of the reaction in ethanol by varying the catalyst. The temperature and catalytic amount also play important roles in the yield and ee of the reaction.[57,58] We performed the nitroaldol reaction of *p*-nitrobenzaldehyde as the model substrate at various temperatures, viz., room temperature (rt) and 0, −10, −20, −30, and −40 °C. It can be observed from Table S6 in the Supporting Information that *p*-nitrobenzaldehyde gives a maximum yield and ee at −20 °C. However, the enantioselectivity is found to decrease at −40 °C. This may be due to the fact that, below −20 °C, the reaction intermediate gets stabilized and thereby affects the enantioselectivity. Because we obtained better efficiency of the catalyst at −20 °C, we performed all of the other reactions at this temperature using various Schiff-base complexes (Table 4). As far as the catalytic amount is concerned, we have varied the catalytic amount from 5 to 25 mg, keeping the amount of the substrate constant. With an increase in the catalytic amount from 5 to 10 mg, both the yield (above 90%) and ee (up to 84%, *R* isomer) are found to enhance. However, no significant enhancement in the yield as well as in the enantioselectivity is observed upon further

dx.doi.org/10.1021/ic400599c | *Inorg. Chem.* 2013, 52, 8017−8029

Table 5. Conversion and Selectivity for the Reactions catalyzed by Neat and Encapsulated Copper Schiff-Base Complexes

		Cu(L1)		Cu(L2)		Cu(L1)-Y		Cu(L2)-Y	
reactant	product	% conv	*R*:*S*	% conv	*R*:*S*	% conv	*R*:*S*	% conv	*R*:*S*
1a	**2a**	84	83:17	82	82:18	95	81:19	92	84:16
1b	**2b**	92	93:7	86	88:12	100	95:5	100	93:7
1c	**2c**	90	90:10	90	89:11	100	92:8	98	97:3
1d	**2d**	82	81:19	88	74:26	97	90:10	87	86:14
1e	**2e**	85	84:16	80	64:37	90	94:6	87	82:18
1f	**2f**	86	86:14	85	62:38	88	75:25	85	78:22

increment of the catalytic amount. So, we choose 10 mg of the catalyst to be the optimal amount.

After optimization of the solvent, temperature, and amount of catalyst, the scope of the nitroaldol reaction with supported catalysts is extended to various other substituted benzaldehydes under the above optimized reaction conditions (Table 4). The percent of conversion and selectivity (*R*:*S* ratio) of the reactions is given in Table 5. To compare the catalytic activity of the homogeneous and heterogeneous catalysts, time versus conversion plots for the reactions of 2- and 4-nitrobenzaldehyde are shown as representative cases in Figure 7.

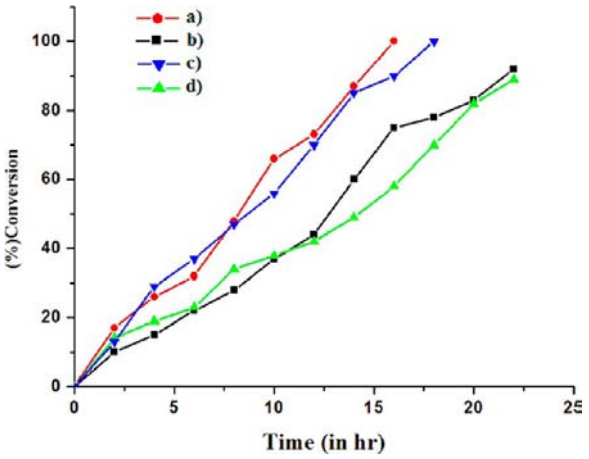

Figure 7. Plot of (%) conversion versus time for condensation of 4-nitrobenzaldehyde with nitromethane catalyzed by (a) Cu(L1)-Y and (b) Cu(L1) complexes. Plot of (%) conversion versus time for the reaction of 2-nitrobenzaldehyde with nitromethane catalyzed by (c) Cu(L1)-Y and (d) Cu(L1).

It can be seen from Tables 4 and 5 that the heterogeneous chiral catalyst gives almost 100% conversion with high enantioselectivity. As far as the mass balance is concerned, there appears to be some mass imbalance in the reaction, especially with the reaction catalyzed by the homogeneous catalyst. This is due to the fact that about 10−15% percent of aldehydes remains unconverted to the desired product and about 2−5% of the product gets decomposed or oxidized during column separation. At a glimpse, all of the chiral complexes encapsulated into the zeolite cavities used in the present study give good yield and ee in the nitroaldol reaction of a wide range of substrates. The substrates with electron-withdrawing groups, for example, 2- and 4-nitrobenzaldehyde, gave higher enantioselectivities in comparison to other substrates. It can be observed from Table 4 that zeolite-encapsulated complexes show better catalytic efficiency than their homologous analogues. Out of the two heterogeneous catalysts, the Cu(L1)-Y catalyst preferably shows the highest catalytic activity. The enhancement of the catalytic activity upon encapsulation into the zeolite cavity can be attributed to chiral enhancement due to the confinement effect associated with the supercage of zeolite-Y. It is also reported that, by anchoring or immobilizing the catalysts onto microporous and mesoporous materials, there is a significant increase in ee compared to that of its homogeneous analogue.[27,59−61] The increase in the catalytic ability of these catalysts can also be correlated with our theoretical results. Because our theoretical calculation suggests that upon encapsulation the global hardness decreases, according to Pearson's HSAB principle,[62,63] they become more reactive in nature. Moreover, the f_κ^+ value, which indicates the preferential site for a nucleophilic attack, is mostly concentrated at the Cu center in the encapsulated complexes (Figure S10 in the Supporting Information). Also, as stated by Evan et al.,[21] after generation of the nitronate ion, this nucleophile binds to the Cu center through one of the O atoms. So, values of the FF suggest that among our systems this step becomes more feasible in the case of the Cu(L1)-Y-encapsulated complex having a maximum f_κ^+ value, followed by Cu(L2)-Y, Cu(L2), and Cu(L1), respectively. Furthermore, from our DFT calculation, it is evident that the HOMO−LUMO gap (ΔE = 0.493 eV) and global hardness value (η = 0.246 eV) in the intermediate complex [Cu(L1)-Y + CH_2NO_2] formed inside the cavity of zeolite-Y are much less in comparison to those of the homogeneous counterparts (ΔE = 1.012 eV and η = 0.506 eV; Figure 8). This result indicates that the reaction intermediates formed in the heterogeneous catalytic system are much more reactive than those of the homogeneous counterparts. The decrease in the HOMO−LUMO gap and global hardness value in the Cu(L1)-Y + CH_2NO_2 complex satisfactorily explains the facts for the faster catalytic performance of the nitroaldol reaction inside the cavity of zeolite-Y. In other words, it can be said that the zeolite matrix highly influences the catalytic ability of the copper Schiff-base complexes.

In order to examine the roles of the Schiff-base moiety of the catalytic activity, we performed the nitroaldol reaction in the presence of NaY and Schiff-base ligands. Herein again we consider the reaction of *p*-nitrobenzaldehyde as the model system. In the presence of NaY, the maximum percent yield is found to be 54% with a racemic mixture of the product. Upon the addition of the chiral ligand system into the reaction media, the yield is found to increase from 50% to 60% and the ee (%) is found to be 45%. This revealed that the presence of a chiral Schiff-base ligand is critical for reaction efficiency and is essential to impart enantioselectivity of the product. We have also tested the reaction of *p*-nitrobenzaldehyde with the L1 ligand without a NaY or copper source. The reaction was found to be sluggish with a low percent yield although 40% enantioselectivity in the product is obtained. The results of the nitroaldol reaction performed only in the presence of a

dx.doi.org/10.1021/ic400599c | Inorg. Chem. 2013, 52, 8017−8029

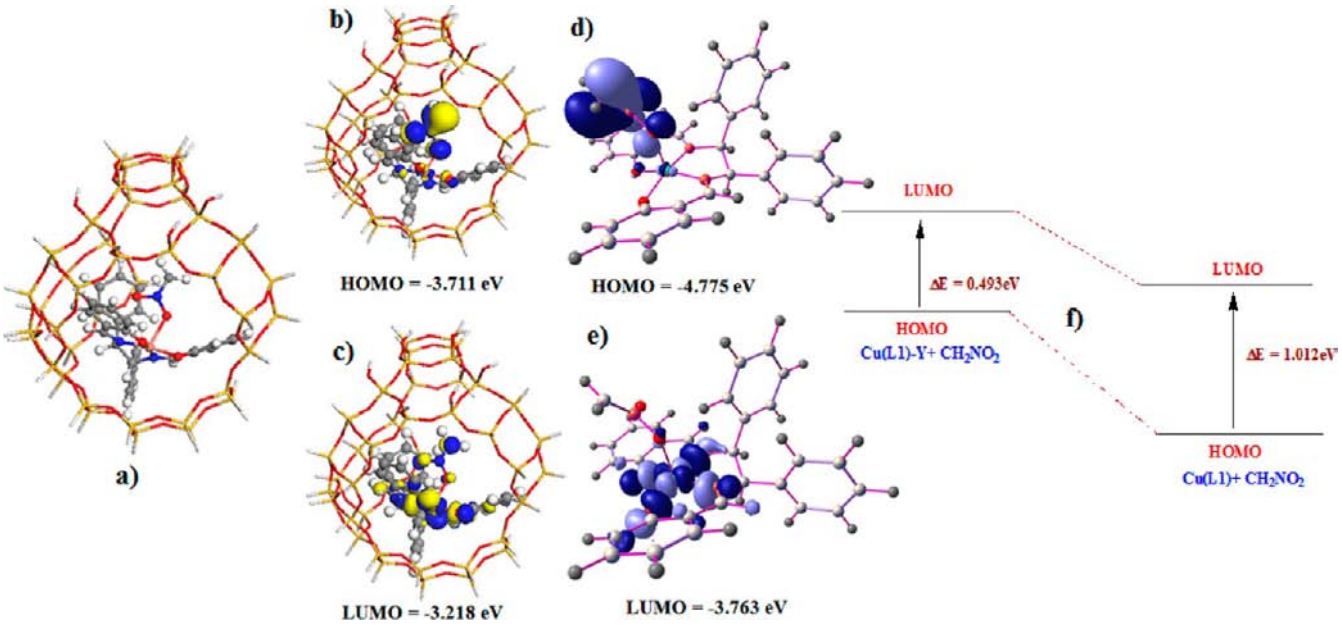

Figure 8. (a) Optimized geometry of Cu(L1)-Y with the nucleophile $CH_2NO_2^-$. (b) HOMO of Cu(L1)-Y + CH_2NO_2. (c) LUMO of Cu(L1)-Y + CH_2NO_2. (d) HOMO of Cu(L1) + CH_2NO_2. (e) LUMO of Cu(L1)-Y + CH_2NO_2. (f) HOMO−LUMO gap in neat and encapsulated intermediate complexes.

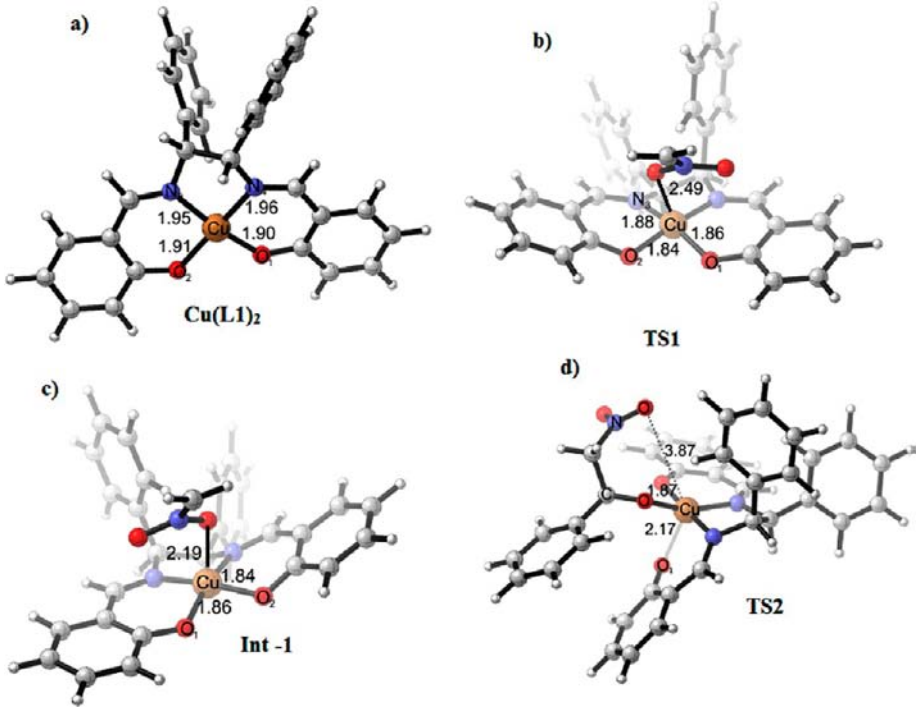

Figure 9. Optimized geometries of possible intermediate and transition states involved in the catalytic cycle.

chiral Schiff-base ligand (L1) under different solvent conditions are shown in Table S7 in the Supporting Information.

The synthesized heterogeneous chiral catalysts are found to be effective up to six cycles without any leaching of the metal complexes. The amount of the copper content in the catalyst is determined by Vogel's[46] method after recovery of the catalyst. The amount of the copper content in the catalysts is found to be the same up to six cycles. However, after the sixth cycle, the copper content is found to be less. The amounts of metal content losses after the sixth cycle are given in Table S8 in the Supporting Information.

3.12. Plausible Mechanism of the Henry Reaction Catalyzed by the Cu(L1) Complex. An attempt has been made to rationalize the plausible pathway involved in the catalytic conversion. The catalytic cycle is depicted in Scheme S3 in the Supporting Information. Because Cu(L1)-Y is found to be a better catalyst, for the mechanistic study, we choose the neat Cu(L1) complex. The catalytic cycle is supposed to involve three steps. The first step involves abstraction of a

dx.doi.org/10.1021/ic400599c | Inorg. Chem. 2013, 52, 8017−8029

methyl proton from nitromethane with acetate acting as a base,[19] generating the nitronate ion. The second step involves coordination of the nitronate ion to the Cu center via a Cu−O−N linkage. The third step involves the simultaneous attack of the nucleophile to the incoming aldehyde and formation of an activated complex followed by the release of the product. To support this mechanism, we perform DFT calculations on the possible intermediate and transition states. The optimized geometry of Cu(L1), possible transition states, and reaction intermediates are shown in Figure 9. The energy profile for this three-step reaction is shown in Figure 10. It can be seen from

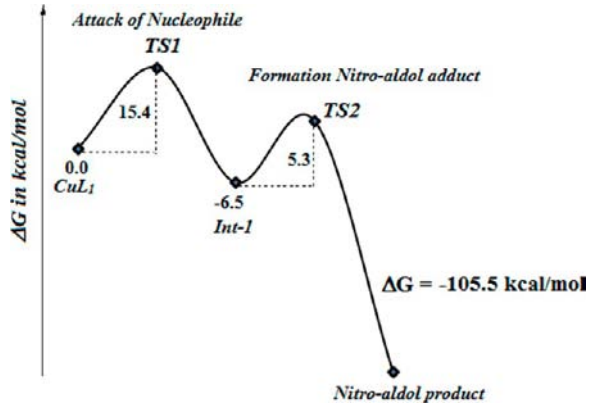

Figure 10. Simple energy profile diagram for catalytic conversion.

Figure 9 that as the nitronate ion coordinates to the Cu center the square-planar complex undergoes a Jahn−Teller distortion with compression of the Cu−O and Cu−N bonds. This step is endergonic in nature, has to cross an energy barrier of 15 kcal/mol to form the intermediate state 1 (Int-1), and is the rate-determining step. In both the transition and intermediate states, the incoming nucleophile is found to lie in the axial position with Cu−O bond distances of 2.44 and 2.19 Å, respectively. During this process, the unpaired electron on the Cu center gets coupled with the unpaired electron of the O atom of nitronate. This is in accordance with our ESR analysis and spin density calculation. Once the metal complex undergoes radical coupling, it becomes ESR-inactive. Because spin density calculations predict the unpaired electron to be concentrated mostly on the Cu center, the incoming nucleophile will have a higher tendency to get attached to the Cu center. Further, from our DFT calculation, it is predicted that if the electron spin in the d_{xy} orbital is in the downward direction, the complex becomes more reactive. Therefore, the most favored situation for d−p mixing between the Cu center and nitronate in the TS1 or Int-1 will be the one in which the unpaired electron in d_{xy} aligns in the downward direction [Scheme S3(ii) in the Supporting Information]. Upon the addition of the aldehydes, the nucleophile bonded to the Cu center attacks the C atom of the aldehydic group and finally leads to the formation of the product. Upon going from Int-1 to the nitroaldol product, Int-1 passes through a transition state (TS2) and has to cross an energy barrier of 5.3 kcal/mol. In TS2, the square-planar copper complex undergoes a Berry pseudorotation, allowing the O atom of the incoming aldehyde to bind from the equatorial position. At this stage, there occurs a large elongation of the Cu−O_1 bond (due to Jahn−Teller distortion) and the nitronate moves away from the ligand plane to lie perpendicular to the plane. The calculated transition state geometry is similar to the type proposed recently by Dhahagani et al.[23] It is evident that, for those complexes that simultaneously bind both an electrophile and a nucleophile, the most reactive transition state is the one in which the nucleophile lies perpendicular to the ligand plane, while the electrophile resides in the equatorial sites of the ligand plane.[21] This statement is in good agreement to our theoretical observation. By this argument, it can be said that TS2 will exhibit the highest reactivity. After formation of the reaction intermediate complex, formation of the product is greatly favored, as indicated by a high negative value of ΔG = −105.5 kcal/mol (Figure 10).

4. CONCLUSION

The chiral Schiff-base complexes of copper encapsulated inside zeolite-Y are found to be better catalysts in terms of the thermal stability and catalytic efficiency. The catalytic ability of these complexes is found to depend on the temperature, solvent system, and catalytic amount. Low temperatures up to −20 °C, high polarity of the solvent, and low catalytic amount gives the highest enantioselectivity. DFT calculation predicts that encapsulation reduces the global hardness and increases the softness and FF values of the complexes, resulting in higher catalytic ability of the encapsulated complexes. Further, it is revealed from our theoretical calculation that in the catalytic cycle (TS2) the nucleophile must reside in the axial position and the electrophile should be positioned in the equatorial site of the ligand plane for better catalytic performance.

■ ASSOCIATED CONTENT

Supporting Information

Details of the experimental and theoretical methods, characterization techniques, EDX spectra of zeolite-Y-encapsulated complexes, UV−vis/DRS data, UV/DRS of Cu^{2+}-exchanged zeolite, redox potential values, XPS spectra, SEM, and TGA, FF analysis, correlation between IP versus HOMO energy and EA versus LUMO, results of the Henry reaction at different temperatures, in different solvents, and in the presence of ligand L1 alone, leaching study, mechanism of the reaction, ^{1}H and ^{13}C NMR, and HPLC data of nitroaldol products and synthetic ligand. This material is available free of charge via the Internet at http://pubs.acs.org.

■ AUTHOR INFORMATION

Corresponding Author

*E-mail: ramesh@tezu.ernet.in.

Notes

The authors declare no competing financial interest.

■ ACKNOWLEDGMENTS

The authors thank the Department of Science and Technology, New Delhi, India, for financial support.

■ REFERENCES

(1) Kervinen, K.; Pieter, C. A. B.; Andrew, M. B.; Gerbrand Mesu, J. G.; Koten, G.; Robertus, J. M. K. G.; Weckhuysen, B. M. *J. Am. Chem. Soc.* **2006**, *128*, 3208−3217.

(2) Modi, C. K.; Trivedi, P. M.; Gupta, S. K.; Jha, P. K. *J. Inclusion Phenom. Macrocyclic Chem.* **2012**, *74*, 117−127.

(3) Zhu, D.; Mei, F.; Chen, L.; Li, T.; Mo, W.; Li, G. *Energy Fuels* **2009**, *23*, 2359−2363.

(4) Bania, K. K.; Bharali, D.; Viswanathan, B.; Deka, R. C. *Inorg. Chem.* **2012**, *51*, 1657−1674.

(5) Corma, A.; Garcia, H. *Eur. J. Inorg. Chem.* **2004**, 1143−1164.

(6) Diegruber, H.; Plath, P. J.; Schultz-Elkoff, E. G.; Mohl, M. *J. Mol. Catal.* **1984**, *24*, 115−126.
(7) Herron, N. *Inorg. Chem.* **1986**, *25*, 4714−4717.
(8) Xuereb, D. J.; Raja, R. *Catal. Sci. Technol.* **2011**, *1*, 517−534.
(9) Bania, K. K.; Deka, R. C. *J. Phys. Chem. C* **2011**, *115*, 9601−9607.
(10) Bania, K. K.; Deka, R. C. *J. Phys. Chem. C* **2012**, *116*, 14295−14310.
(11) Collis, A. E. C.; Horváth, I. T. *Catal. Sci. Technol.* **2011**, *1*, 912−919.
(12) Alcón, M. J.; Corma, A.; Iglesias, M.; Sánchez, F. *J. Organomet. Chem.* **2002**, *655*, 134−145.
(13) Mori, K.; Kawashima, M.; Kagohara, K.; Hiromi Yamashita, H. *J. Phys. Chem. C* **2008**, *112*, 19449−19455.
(14) Mori, K.; Kawashima, M.; Kagohara, K.; Hiromi Yamashita, H. *J. Phys. Chem. C* **2008**, *112*, 2593−2600.
(15) Corrêa, R. J.; Salomão, G. C.; Olsen, M. H. N.; Filho, L. C.; Drago, V.; Fernandes, C.; Antunes, O. A. C. *Appl. Catal., A* **2008**, *336*, 35−39.
(16) Poltowicz, J.; Pamin, K.; Tabor, E.; Haber, J.; Adamski, A.; Sojka, Z. *Appl. Catal., A* **2006**, *299*, 235−242.
(17) Baleizão, C.; Garcia, H. *Chem. Rev.* **2006**, *106*, 3987−4043.
(18) Herron, N. *Biocatalysis and Biomimetics*; ACS Symposium Series 392; American Chemical Society: Washington, DC, 1989; Chapter 11, pp 141−154.
(19) (a) Rosini, G. In *Comprehensive Organic Synthesis*; Trost, B. M., Ed.; Pergamon: Oxford, U.K., 1996; Vol. 2, p 321. (b) Luzzio, F. A. *Tetrahedron* **2001**, *57*, 915−945. (c) Ono, N. *The Nitro Group in Organic Synthesis*; Wiley-VCH: New York, 2001; Chapter 3, p 30.
(20) (a) Sasai, H.; Suzuki, T.; Arai, S.; Shibasaki, M. *J. Am. Chem. Soc.* **1992**, *114*, 4418−4420. (b) Shibasaki, M.; Yoshikawa, N. *Chem. Rev.* **2002**, *102*, 2187−2209 and references cited therein.
(21) Evans, D. A.; Seidel, D.; Rueping, M.; Lam, H. W.; Shaw, J. T.; Downey, C. W. *J. Am. Chem. Soc.* **2003**, *125*, 12692−12693.
(22) Jacobsen, E. N.; Zhang, W.; Muci, A. R.; Ecker, J. R.; Deng, L. *J. Am. Chem. Soc.* **1991**, *113*, 7063−7064.
(23) Dhahagani, K.; Rajesh, J.; Kannan, R.; Rajagopal, G. *Tetrahedron: Asymmetry* **2011**, *22*, 857−865.
(24) Cheng, H. G.; Lu, L. Q.; Wang, T.; Chen, J. R.; Xiao, W. J. *Chem. Commun.* **2012**, *48*, 5596−5598.
(25) Ogunwumi, S. B.; Bein, T. *Chem. Commun.* **1997**, 901−902.
(26) Sabater, M. J.; Corma, A.; Domenech, A.; Fornés, V.; García, H. *Chem. Commun.* **1997**, 1285−1286.
(27) Thomas, J. M.; Raja, R. *Acc. Chem. Res.* **2008**, *41*, 708−720.
(28) Yang, H. Q.; Zhang, L.; Zhong, L.; Yang, Q. H.; Li, C. *Angew. Chem., Int. Ed.* **2007**, *46*, 6861−6865.
(29) Jones, M. D.; Raja, R.; Thomas, J. M.; Johnson, B. F. G.; Lewis, D. W.; Rouzaud, J.; Harris, K. D. M. *Angew. Chem., Int. Ed.* **2003**, *42*, 4326−4331.
(30) Li, C. *Catal. Rev. Sci. Eng.* **2004**, *46*, 419−492.
(31) (a) Quayle, W. H.; Lunsford, J. H. *Inorg. Chem.* **1982**, *21*, 97−103. (b) Quayle, W. H.; Peeters, G.; DeRoy, G. L.; Vansant, E. F.; Lunsford, J. H. *Inorg. Chem.* **1982**, *21*, 2226−2231.
(32) Jin, C.; Fan, W. B.; Jia, Y. J.; Fan, B. B.; Ma, J. H.; Li, R. F. *J. Mol. Catal. A: Chem.* **2006**, *249*, 23−30.
(33) Bessel, C. A.; Rolison, D. R. *J. Phys. Chem. B* **1997**, *101*, 1148−1157.
(34) Reddy, B. M.; Rao, K. N.; Bharali, P. *Ind. Eng. Chem. Res.* **2009**, *48*, 8478−8486.
(35) Mozo, E P.; Cabrimas, N.; Lucaccioni, F.; Acosta, D. D.; Patron, P.; Cmestra, A. L.; Ruiz, P.; Delmon, B. *J. Phys. Chem.* **1993**, *97*, 12819−12827.
(36) Jafarian, M.; Rashvandavei, M.; Khakali, M.; Gobal, F.; Rayati, S.; Mahjani, M. G. *J. Phys. Chem. C* **2012**, *116*, 18518−18532.
(37) Senaratne, C.; Zhang, J.; Baker, M. D.; Bessel, C. A.; Rolison, D. R. *J. Phys. Chem.* **1996**, *100*, 5849−5862.
(38) Shaw, B. R.; Creasy, K. E.; Lanczycki, C. J.; Sargeant, J. A.; Tirhado, M. *J. Electrochem. Soc.* **1988**, *135*, 869−876.
(39) Dutta, P. K.; Ledney, M. *Prog. Inorg. Chem.* **1997**, *44*, 209−271.
(40) Doménech, A.; Formentín, P.; García, H.; Sabater, M. J. *J. Phys. Chem. B* **2002**, *106*, 574−582.
(41) Bessel, C. A.; Rolison, D. R. *Stud. Surf. Sci. Catal.* **1995**, *98*, 114−115.
(42) Cassidy, J.; Breen, W.; O'Donoghue, E.; Lyons, M. E. G.. *Electrochim. Acta* **1991**, *36*, 383−384.
(43) Bedioui, F.; Roué, L.; Briot, E.; Devynck, J.; Bell, S. L.; Balkus, K. J., Jr. *J. Electroanal. Chem.* **1994**, *373*, 19−29.
(44) Bessel, C. A.; Rolison, D. R. *J. Phys. Chem. B* **1997**, *101*, 1148−1157.
(45) Viswanathan, B.; Ganesan, R. *J. Phys. Chem. B* **2004**, *108*, 7102−7114.
(46) Vogel, A. I. *Textbook of Quantitative Chemical Analysis*, 6th ed.; Pearson Education: London, 2002; p 393.
(47) Silva, M.; Freire, C.; de Castro, B.; Figueiredo, J. L. *J. Mol. Catal. A: Chem.* **2006**, *258*, 327−333.
(48) Singh, K.; Kumar, Y.; Puri, P.; Kumar, M.; Sharma, C. *Eur. J. Med. Chem.* **2012**, *52*, 313−321.
(49) *MaterialsStudio 4.3*; Accelrys Software Inc.: San Diego, CA, 2008.
(50) Calabro, D. C.; Lichtenberger, D. L. *Inorg. Chem.* **1980**, *19*, 1732−1734.
(51) Bally, T.; Nitsche, S.; Roth, K.; Haselbach, E. *J. Am. Chem. Soc.* **1984**, *106*, 3927−3933.
(52) Jano, I. *J. Phys. Chem.* **1991**, *95*, 7694−7699.
(53) Schildcrout, S. M.; Pearson, R. G.; Stafford, F. E. *J. Am. Chem. Soc.* **1968**, *90*, 4006−4010.
(54) Parr, R. G.; Chattaraj, P. K. *J. Am. Chem. Soc.* **1991**, *113*, 1854−1855.
(55) Chattaraj, P. K.; Liu, G. H.; Parr, R. G. *Chem. Phys. Lett.* **1995**, *237*, 171−176.
(56) Morell, G.; Labet, V.; Granda, A.; Chermetteb, H. *Phys. Chem. Chem. Phys.* **2009**, *11*, 3417−3423.
(57) Cruz, A. J.; Pires, J.; Carvalho, A. P.; de Carvalho, M. B. *J. Chem. Eng. Data* **2004**, *49*, 725−731.
(58) Park, J.; Lang, K.; Abboud, K. A.; Hong, S. *J. Am. Chem. Soc.* **2008**, *130*, 16484−16485.
(59) Trost, B. M.; Yeh, V. S. C. *Angew. Chem., Int. Ed.* **2002**, *41*, 861−863.
(60) Prasetyanto, E. A.; Lee, S.-C.; Jeong, S.-M.; Park, S.-E. *Chem. Commun.* **2008**, *17*, 1995−197.
(61) Prasetyanto, E. A.; Jeong, S.-M.; Park, S.-E. *Top. Catal.* **2010**, *53*, 192−199.
(62) Mauryaa, M. R.; Chandrakar, A. K.; Chand, S. *J. Mol. Catal.* **2007**, *274*, 192−201.
(63) Pearson, R. G. *Chemical Hardness: Applications from Molecules to Solids*; Wiley-VCH Verlag Gmbh: Weinheim, Germany, 1997.